![Victoria University Melbourne Australia logo]

Tuning nanofiltration membrane performance: OH–MoS2 nanosheet engineering and divalent cation influence on fouling and organic removal

This is the Published version of the following publication

Mallya, Deepak Surendhra, Yang, Guoliang, Lei, Weiwei, Muthukumaran, Shobha and Baskaran, Kanagaratnam (2023) Tuning nanofiltration membrane performance: OH–MoS2 nanosheet engineering and divalent cation influence on fouling and organic removal. Discover Nano, 18. ISSN 2731-9229

Discover Nano

Discover

Research

Tuning nanofiltration membrane performance: OH–MoS$_2$ nanosheet engineering and divalent cation influence on fouling and organic removal

Deepak Surendhra Mallya[1] · Guoliang Yang[2] · Weiwei Lei[2] · Shobha Muthukumaran[3,4] · Kanagaratnam Baskaran[1]

Abstract

Natural organic matter (NOM) present in surface water causes severe organic fouling of nanofiltration (NF) membranes employed for the production of potable water. Calcium (Ca^{2+}) and magnesium (Mg^{2+}) are alkaline earth metals present in natural surface water and severely exacerbate organic fouling owing to their ability to cause charge neutralization, complexation, and bridging of NOM and the membrane surface. Hence, it is of practical significance to engineer membranes with properties suitable for addressing organic fouling in the presence of these cations. This study employed OH-functionalized molybdenum disulphide (OH–MoS$_2$) nanosheets as nanofillers via the interfacial polymerization reaction to engineer NF membranes for enhanced removal of NOM and fouling mitigation performance. At an optimized concentration of 0.010 wt.% of OH–MoS$_2$ nanosheet, the membrane was endowed with higher hydrophilicity, negative charge and rougher membrane morphology which enhanced the pure water permeance by 46.33% from 11.2 to 16.39 L m^{-2} h^{-1} bar^{-1} while bridging the trade-off between permeance and salt selectivity. The fouling performance was evaluated using humic acid (HA) and sodium alginate (SA), which represent the hydrophobic and hydrophilic components of NOM in the presence of 0, 0.5, and 1 mM Ca^{2+} and Mg^{2+}, respectively, and the performance was benchmarked with control and commercial membranes. The modified membrane exhibited normalized fluxes of 95.09% and 93.26% for HA and SA, respectively, at the end of the 6 h filtration experiments, compared to the control membrane at 89.71% and 74.25%, respectively. This study also revealed that Ca^{2+} has a more detrimental effect than Mg^{2+} on organic fouling and NOM removal. The engineered membrane outperformed the commercial and the pristine membranes during fouling tests in the presence of 1 mM Ca^{2+} and Mg^{2+} in the feed solution. In summary, this study has shown that incorporating OH–MoS$_2$ nanosheets into membranes is a promising strategy for producing potable water from alternative water sources with high salt and NOM contents.

Keywords Natural organic matter · Nanofiltration membranes · Organic fouling · MoS$_2$ nanosheet · Calcium ion · Magnesium ion

Introduction

With the increased demand for potable water, new membrane-based water purification materials are being extensively developed [1]. Nanofiltration (NF) membranes are promising single-step treatment methods that offer a resourceful approach to meet multiple water quality guidelines and facilitate the removal of natural organic matter (NOM), inorganic matter, micropollutants, heavy metals, and microorganisms during potable water production [1, 2]. In general, NF membrane separation performance is primarily governed by a combination of membrane properties, including electrostatic interactions, size exclusion, and hydrophobic/hydrophilic interactions, as well as the feed water chemistry and filtration conditions such as pressure, crossflow velocity, and temperature [3]. NF membranes have been widely used for potable water production from groundwater and surface water sources [4]. Although NF membranes have demonstrated superior performance compared to conventional treatment alternatives, such as coagulation, adsorption, and medium filtration, membrane fouling remains a significant challenge for water treatment facilities [5]. Significant research efforts have focused on understanding the fouling mechanisms, membrane–foulant interactions, and influencing factors, as well as the synthesis of next-generation engineered membranes for fouling mitigation [6, 7].

Organic fouling is primarily caused by the abundance of natural organic matter (NOM) in the water sources. NOM is problematic because it causes pore blockage of the membranes, significantly reducing permeance and deteriorating separation performance, as well as membrane structural integrity [6]. Furthermore, during the disinfection stage of water treatment, NOM reacts with disinfectants to form a suite of carcinogenic disinfection by-products (DBPs) [8]. NF membranes have proven to be very effective in removing various NOM fractions and supporting the production of safe drinking water [5]. A commercial XN45 NF membrane removed > 70% of NOM as dissolved organic carbon (DOC), compared to a conventional water treatment plant at 57.5% [9]. The membranes also performed exceedingly well in removing 87% and 92% of humic and building blocks, respectively, and significantly lowered the permeate chlorine demand and hazards associated with DBPs [9]. Although NF membranes are versatile in handling the NOM problem, the increasing concentration of NOM due to anthropogenic activities and adverse climate change effects, along with the diverse interactions of NOM with cations such as calcium (Ca^{2+}) and magnesium (Mg^{2+}) in natural water, aggravates the organic fouling problem [5]. The concentrations of Ca^{2+} and Mg^{2+} vary according to the specific region and are influenced by land type, geochemical structure, land use, biogeochemical cycles, and catchment management [10, 11]. In general context, the concentration ranges of Ca^{2+} and Mg^{2+} in surface water are between 0.5 and 2 mM [12].

Various characteristics of NOM, including its size, charge, and polarity, govern its fouling behaviour during NF. Several researchers have focused on evaluating the fouling performance of NF membranes instigated by humic acid (HA) and sodium alginate (SA) fractions of NOM [10, 13, 14]. HA represents the hydrophobic fraction of NOM, which contains large molecules rich in aromatic carbon, as well as functional groups such as carboxyl and phenols [15]. SA represents polysaccharide components with similar behaviour to the extracellular polymeric substance fraction of NOM, which are widely present in various natural waters, causing more severe fouling problems [16]. Cations such as Ca^{2+} and Mg^{2+} affect NOM properties via interactions through electrostatic charge, complex formation, and bridging with deprotonated groups of NOM and the membrane surface [3]. NOM fractions, including HA and SA, facilitate the formation of combined crystal organic aggregates, increase the gelling tendency, and act as nuclei to enhance bulk crystallization, leading to scaling and precipitation [17, 18]. The polysaccharide fraction of NOM, such as SA, has a rigid fibrous structure that forms an extensive three-dimensional crosslinked structure in the presence of Ca^{2+}, significantly increasing the deposition of a dense fouling layer on the membrane surface and deteriorating NF performance [12]. Hence, there is a critical need to develop a fouling-resistant NF membrane to address this growing complex NOM issue.

Advances in membrane science and technology have resulted in the development of next-generation two-dimensional (2D) nanosheet-engineered thin-film nanocomposite (TFN) NF membranes via interfacial polymerization (IP) with enhanced organic removal and antifouling performance [19, 20]. 2D-enabled TFN NF membranes incorporated with nanosheets, such as molybdenum disulphide (MoS_2) [21], metal carbides and nitrides (MXene) [22], and graphitic carbon nitride (g-C_3N_4) [23], exhibit enhanced water permeance, selectivity, and high organic fouling resistance. Among these emerging 2D nanosheets, MoS_2 is a promising material for tailoring membranes with enhanced fouling resistance, while bridging the trade-off between permeance and selectivity [20]. MoS_2 is a typical transition metal chalcogenide with Mo and S atoms forming hexagonal layered structures. Engineering the membrane surface with

MoS_2 nanosheets via the IP reaction resulted in careful control of the surface properties, including wettability, streaming potential, and surface morphology, imparting enhanced antifouling properties [24, 25]. In our previous study, we comprehensively evaluated the impact of OH-functionalized MoS_2 (OH–MoS_2) nanosheets as engineering material during the synthesis of polypiperazine amide (PPA) skin layer via the IP process [26]. The engineered membranes with an optimum concentration of 0.010 wt.% OH–MoS_2 nanosheets resulted in 45.17% increase in pure water flux at 84.14 L m^{-2} h^{-1} against the control membrane at 57.96 L m^{-2} h^{-1}, while retaining excellent salt rejection of 96.67% for Na_2SO_4. OH–MoS_2-engineered membrane showed enhanced fouling resistance and organic removal during filtration studies with the HA feed solution. Although several studies have evaluated the organic fouling performance of TFN membranes, most have focused on using very high concentrations of NOM to accelerate fouling; however, this does not represent the behaviour of NOM-containing surface water [27–30]. Hence, there is a critical gap in the literature regarding the performance analysis of TFN NF membranes during filtration tests with hydrophobic and hydrophilic organic fractions at concentrations similar to natural surface water with cations, such as Ca^{2+} and Mg^{2+} [4, 25, 31].

In this study, 0.010 wt.% OH–MoS_2 nanosheets were used to engineer PPA membrane via optimized IP reaction conditions for high organic fouling resistance. Notably, the IP reaction parameters were further optimized from our previous study to facilitate enhanced fouling resistance and NOM removal during filtration experiments with hydrophobic and hydrophilic fractions of NOM [26]. The properties to performance relationships of the engineered membranes were evaluated through extensive material characterizations. Filtration studies were conducted using lab-prepared feed solutions of HA and SA, which are synthetic surrogates of hydrophobic and hydrophilic organic fractions, respectively, with similar levels present in natural surface water. The impact of Ca^{2+} and Mg^{2+} on NOM removal and fouling performance were systematically evaluated via fouling experiments and the characterization of fouled membranes.

Materials and methods

Materials

Flat sheet polyethersulfone (PES) ultrafiltration (UF) membranes with a molecular weight cut-off (MWCO) of 50 kDa were procured from RisingSun Membrane Technology Co., Ltd. (China), cellulose nitrate (CN) membranes with a 0.45 μm pore size were purchased from Microanalytix Pty Ltd. (Australia), and commercial Trisep XN45 NF membranes were provided by Sterlitech. Inc., (USA). Chemicals including piperazine (PIP, ≥ 99%), trimesoylchloride (TMC, ≥ 98%), triethylamine (TEA), camphorsulfonic acid (CSA), sucrose, h-MoS_2 powder (< 2 μm, 98%), sodium salt of HA, sodium alginate, and dialysis tubes with MWCO of 3500 Da were supplied by Sigma Aldrich (USA). n-Hexane, hydrochloric acid (32%), sodium hydroxide, calcium chloride, magnesium chloride, and sodium chloride were purchased from Merck (Australia). Deionized (DI) water was used to prepare the organic feed solutions employed in the filtration experiments.

Synthesis of OH–MoS_2 nanosheets

OH–MoS_2 nanosheets were synthesized via a simple single-step mechanochemical exfoliation using sucrose and bulk MoS_2 powder [26, 32]. Bulk MoS_2 powder and sucrose in a weight ratio of 1:50 were mixed in a planetary ball mill (Pulverisette 7, Fritsch) at ambient temperature under a nitrogen atmosphere. The ball milling was conducted for 3 h at 400 rpm. At the end of the ball milling process, the OH–MoS_2 nanosheets were dispersed in ultrapure water and dialyzed for 7 days to eliminate the unreacted sucrose. Finally, hydrophilic and ultra-small OH–MoS_2 nanosheets in water were obtained. The protocol used for the nanosheet synthesis is shown in Fig. 1a.

Synthesis of NF membranes

2D-enabled NF membranes were synthesized via modified IP reaction method abridged from our prior study [26]. The PES support membrane was clamped in a plate-and-frame assembly prior to synthesis. The aqueous phase containing 3 wt.% PIP, 3 wt.% CSA, 3 wt.% TEA, and 0.010 wt.% OH–MoS_2 was allowed to react with the PES support membrane or 2 min. To facilitate homogenized dispersion of nanosheets in the aqueous phase, an ultrasonic cleaner was used at 100 W for 30 min. Subsequently, a soft rubber roller was used to uniformly distribute the aqueous phase over the membrane surface. This was followed by 1 min contact with organic phase containing 0.15 wt.% of TMC in n-Hexane. The IP reaction is facilitated at the interface of the aqueous and organic monomer phases, forming a PPA-selective skin layer. After
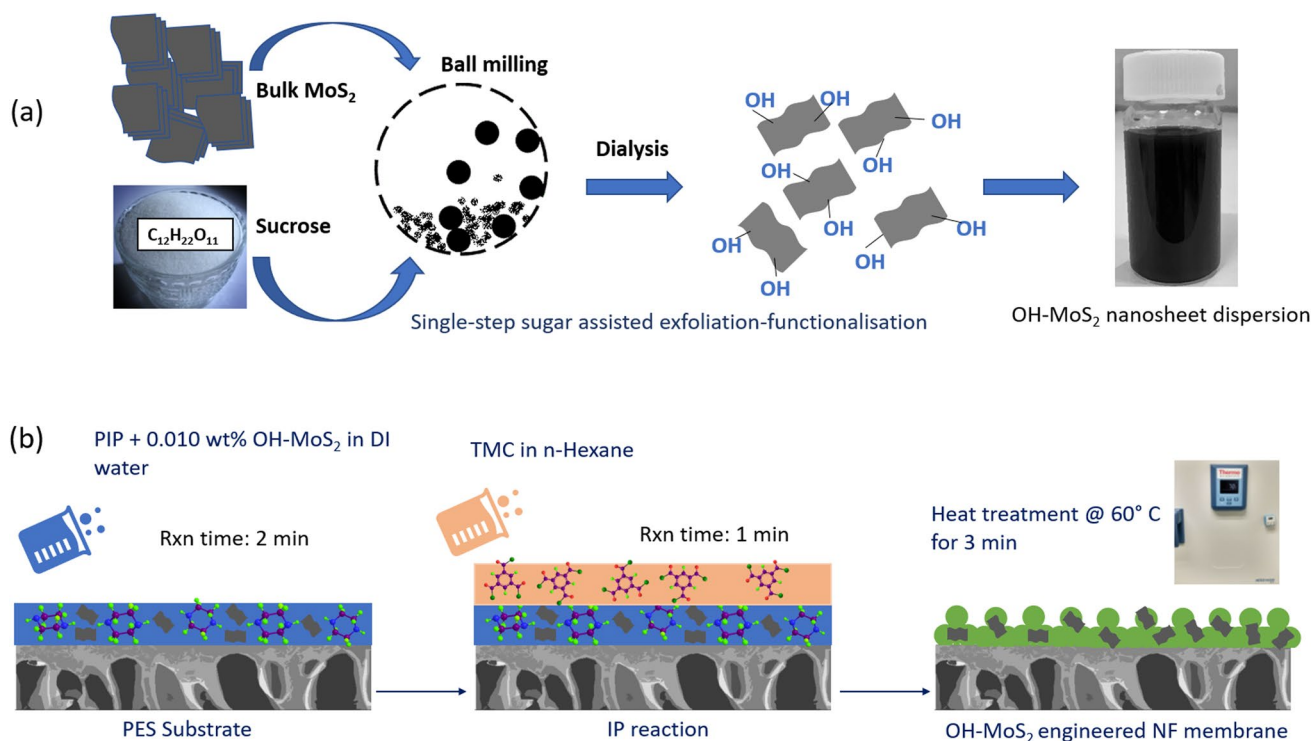
Fig. 1 a Schematic representation of sucrose assisted ball milling procedure for synthesis of OH–MoS$_2$ nanosheets. **b** Schematic of the TFN membrane synthesis protocol used in this study

the IP reaction the organic phase was removed, and the membrane was subsequently washed with n-hexane. Finally, the membranes were exposed to heat treatment at 60 °C for 3 min in a digital oven and stored in DI water at 4 °C until use. A schematic of the IP reaction protocol used in this study is represented in Fig. 1b. Control membranes without the nanosheets were synthesized via similar IP reaction protocol without incorporation of nanosheets in the aqueous phase. The synthesized membranes are termed as control PPA and OH–MoS$_2$ PPA. To benchmark the performance commercial XN 45 membranes were also tested.

Physicochemical characterization of nanosheets and membranes

The physicochemical properties of the nanosheets and membranes were analysed with the characterization methods described below and follows the protocol from our previous experimental publication [26]. Prior to the analysis, all membrane samples were dried in a desiccator for 24 h.

The chemical composition of the nanosheets and membranes was evaluated by attenuated total reflectance-Fourier-transform infrared (ATR-FTIR) spectroscopy. For this Bruker Lumos FTIR spectrometer with wavenumbers ranging from 600 to 4000 cm^{-1} and 64 scans with a resolution of 4 cm^{-1} was employed. Atomic force microscopy (AFM) was employed using a Bruker Multimode 8 instrument operating in non-contact mode at room temperature for analysing the morphology of nanosheets and the surface roughness of the membrane. For the tests with nanosheets, the dispersion was diluted to 0.001 mg mL^{-1} and imaged on a mica substrate. Prior to testing, samples were dried at room temperature. The root average arithmetic roughness (R_a) was evaluated for a scanning area of 5 µm × 5 µm for measuring the membrane surface roughness. The surface morphologies of the nanosheets and membranes were analysed using a Supra 55 VP (ZEISS, Germany) field-emission scanning electron microscope (FE-SEM) instrument. For nanosheet analysis, the nanosheet dispersion was diluted to 0.001 mg mL^{-1} and dried over a silicon substrate for imaging. The surface micromorphologies of the membranes were recorded at 5 kV and working distance of 10 mm. Both nanosheet and membrane samples were subjected to gold coating prior to imaging to improve the conductivity of the samples.

KSV Attention-Theta contact angle apparatus was employed to for the analysis of membrane surface hydrophilicity. Three random points on the membrane were chosen for the CA measurements, and the average values were reported. A Surpass 3 Anton Paar Zeta potential analyser was used to measure the streaming potential of the

fabricated membranes with 1 mM NaCl solution as the background electrolyte. The zeta potentials of the nanosheet dispersion and NOM feed solution were evaluated using a Zetasizer Nano ZS (Malvern Instruments). Microscopic images of the air-dried droplets of the NOM feed solutions were obtained using a benchtop optical microscope (Olympus).

Evaluation of NF membrane performance

The NF membrane performance were evaluated based on the experimental procedures developed from published study [26]. The separation performances of the NF membranes were evaluated by employing a Sterlitech CF042 crossflow filtration setup, exposing an active surface area of 0.0042 m^2. First, the membrane compaction was achieved at 8 bar for 3 h, after which the pure water flux was evaluated at 6 bar for 1 h. This was followed with filtration tests using feed solution containing either HA or SA, which represent the hydrophobic and hydrophilic components of NOM, respectively. The experiments were carried out at ambient room temperature of 25 °C. To mimic the surface water conditions, the feed water concentration was maintained at 8 mg L^{-1}, with a pH of 7 ± 0.05 (using 0.1 HCl or NaOH solution). To evaluate the impact of cations on membrane filtration performance, the feed water containing the organic solution was spiked with 0.5 and 1.0 mM Ca^{2+} and Mg^{2+} using $CaCl_2$ and $MgCl_2$, respectively, to mimic the cation concentration in real surface water.

For all the filtration experiments, a HYDRA-CELL pump was used to pump the feed solution, and the flux was calculated using Eq. (1):

$$J = \frac{Q}{A \times t}$$

(1)

where J is the flux (L m^{-2} h^{-1}), Q is the permeate volume (L), A is the active surface area of the membrane (m^2), and t is time (h). The permeance of each membrane was calculated using Eq. (2).

$$WP = \frac{J}{\Delta p}$$

(2)

where WP is the water permeance (L m^{-2} h^{-1} bar^{-1}), and Δp is the pressure difference (bar).

DOC removal was measured using a total carbon analyser (TOC-L, SHIMADZU Corporation, Japan) for sample aliquots of the feed and permeate. The removal values were evaluated using Eq. (3):

$$R(\%) = 1 - \frac{C_p}{C_f}$$

(3)

where R is the removal (%); C_p is the DOC level in the permeate (mg L^{-1} for DOC, cm^{-1} for UV_{254}, and µS cm^{-1} for salt rejection); and C_f is the DOC level in the feed (mg L^{-1} for DOC, cm^{-1} for UV_{254}, and µS cm^{-1} for salt rejection).

To evaluate the antifouling performance of the membranes, the normalized flux was calculated using Eq. (4):

$$N_F = \left(\frac{J_T}{J_0} \right) \times 100\%$$

(4)

where N_F is the normalized flux, J_T is the flux at the termination of the experiment, and J_0 is the initial flux.

At the end 6 h fouling experiments, the membrane coupons were cleaned with pure water for 20 min, after which the relative flux recovery ratio (R_{re}) was evaluated with fresh water according to Eq. (5):

$$R_{re} = \frac{F_{re}}{F_0} \times 100\%$$

(5)

where F_0 is the initial pure water flux prior to the fouling experiments and F_{re} is the pure water flux after cleaning.

The salt rejection of the membranes was evaluated using feed water containing 1000 mg L^{-1} Na_2SO_4, $MgSO_4$, $CaCl_2$, and NaCl. All experiments were conducted in triplicate, and the average values were reported for the membrane performance experiments.
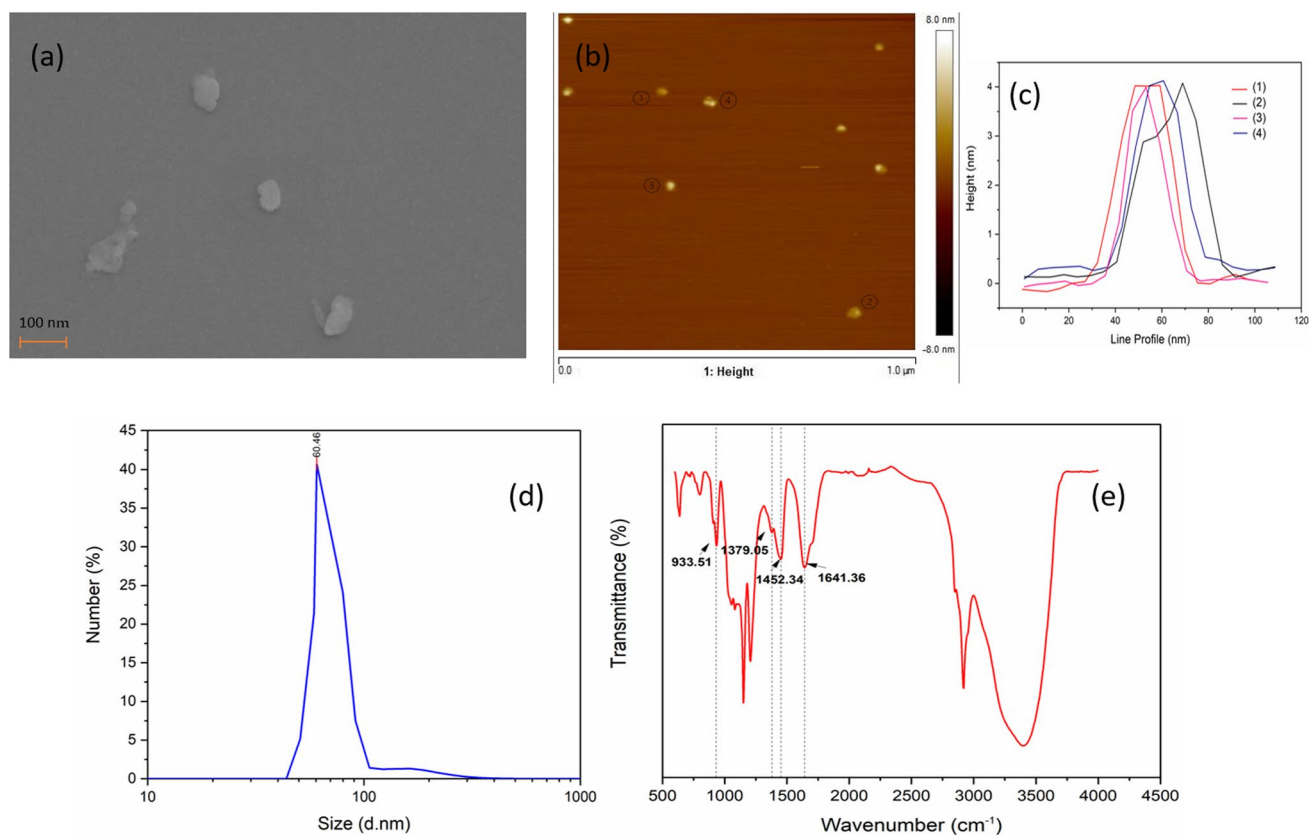
Fig. 2 Characterization of the synthesized OH–MoS$_2$ nanosheets: **a** SEM image, **b** AFM image, **c** corresponding line profiles of nanosheets, **d** average size distribution of nanosheets evaluated using Zetasizer data, and **e** FTIR spectrum of OH–MoS$_2$ nanosheets coated polycarbonate membrane

Results and discussion

Characterization of OH–MoS$_2$ nanosheets

The surface morphologies of the exfoliated OH–MoS$_2$ nanosheets were examined using SEM and AFM. Figure 2a shows the layered structure of OH–MoS$_2$ nanosheets in the size range of 65–91 nm. Additional file 1: Figure S1(a–d) presents SEM images of OH–MoS$_2$ nanosheets at various magnification levels. The average size and thickness of the nanosheets observed by AFM in Fig. 2b, c were ~ 55 nm and ~ 4 nm, respectively, confirming their ultra-small size and 2D few-layered structure. Single layer of MoS$_2$ nanosheet has a thickness of 0.62 nm, and hence, the synthesized OH–MoS$_2$ nanosheets in this study have 6–7 layered structures. The OH–MoS$_2$ nanosheet dispersion exhibited a high zeta potential of − 45.61 mV at pH 7, confirming its hydrophilic nature, while the zetasizer data as shown in Fig. 2d also revealed that the average size distribution of the nanosheets was 60.46 nm. The slight variations in nanosheet size measurements obtained from SEM, AFM, and Zetasizer are expected due to the inherent differences in measurement techniques and conditions. SEM and AFM provide surface-level and topographical insights into nanosheets, respectively, while Zetasizer measures the hydrodynamic size in a solution.

In our study, we employed OH–MoS$_2$ nanosheet dispersion to coat a polycarbonate membrane, and the resulting FTIR spectrum is presented in Fig. 2e. To further substantiate the functionalization of these nanosheets, we have included the FTIR spectra of both the bulk MoS$_2$ powder and the polycarbonate membrane in Additional file 1, Figure S2. Notably, for the bulk MoS$_2$ analysis, we utilized the KBr method to acquire the FTIR data. In Additional file 1: Figure S2, the FTIR spectra of bulk MoS$_2$ powder exhibited prominent peak around 472.54 cm^{-1} which corresponds to the characteristics Mo–S bond vibrations, while the polycarbonate membrane showed notable peaks at 1149.53 cm^{-1} and 1205.46 cm^{-1} corresponding to the symmetric and asymmetric stretching vibrations of C–O–C bond within the

polycarbonate molecule [33, 34]. The FTIR spectra of OH–MoS$_2$ nanosheets (Fig. 2e) present peaks at 1641.36 cm^{-1} and 1452.34 cm^{-1} which corresponds to Mo–S, while the peaks at 933.51 cm^{-1} and 1379.05 cm^{-1} represent S–S and Mo–O bond, respectively [26, 35, 36]. The broad peak ranging between 2900 and 3500 cm^{-1} is due to the symmetric stretching of the hydroxyl groups of the nanosheets [36]. The synthesized MoS$_2$ nanosheets possess ultra-small size, high hydrophilicity, and abundant OH functional groups, facilitating their seamless integration as 2D nanofillers into the polymer matrix, giving rise to a new class of high-performance nanofiltration membranes [26].

Characterization of membranes

FTIR was employed to analyse the chemical compositions of the control PPA and TFN membranes with 0.010 wt.% OH–MoS$_2$ nanosheets, and the results are shown in Fig. 3. Accordingly, for the control PPA membrane, the bands appearing at approximately 1610 cm^{-1} and 1567 cm^{-1} corresponds to the C=O stretching vibration of the amide I bond and the C–N stretching and C–N–H vibrations of the amide II band, respectively, which confirms the formation of a polyamide skin layer [37]. The OH–MoS$_2$ PPA membrane exhibited a redshift of these peaks to 1632 cm^{-1} and 1577 cm^{-1} which could be ascribed to the enhanced IP reaction in the presence of OH–MoS$_2$ and its interaction with the polymer matrix. The OH group grafted on the surface of the nanosheet facilitated hydrogen bonding with the PIP molecules, enhancing the IP reaction and covalent bonding with the unreacted carboxylic groups of the polymer matrix, significantly affecting amide formation [26]. The band at 3200–3600 cm^{-1} and 1485 cm^{-1} could be ascribed to the hydroxyl stretching vibration of the carboxylic groups, whereas the peak at 1570 cm^{-1} could be attributed to the stretching vibration of the benzene ring [38]. In addition, the OH–MoS$_2$ PPA membrane exhibited bands at 640 cm^{-1} and 1375 cm^{-1}, assigned to MoS$_2$ and Mo–O bonds, respectively, confirming the successful incorporation of nanosheets within the polymer matrix [36].

The surface morphologies of the membranes were examined using SEM to determine the impact of OH–MoS$_2$ nanosheets on the membrane surface. As shown in Fig. 4a, XN 45 membrane exhibited a smooth surface with nodular structures. The control PPA membrane (Fig. 4b) exhibited randomly dispersed bubble-like granular structures, which could be related to the swift IP reaction between the monomers. During the IP reaction, the PIP molecules diffuse into interface of aqueous and organic phases and react with TMC, facilitating the formation of a polyamide layer [19]. This extremely thin layer serves as a seeding location to draw additional PIP molecules for polymerization. This can push PPA tufts aside and cause bubble-like nodules to grow on the surface. The local concentration of PIP in the reaction zone controls the density and number of these structures [39]. Engineering the TFN membranes with OH–MoS$_2$ nanosheets at the optimum concentration of 0.010 wt.% resulted in the formation of extensively crumpled fishnet-like structures, as shown in Fig. 4c. This can be related to the local enrichment of PIP molecules via hydrogen bonding with the nanosheets, which promotes the IP reaction around the nanosheets [40].

The hydroxyl groups present on the edges of the OH–MoS$_2$ nanosheets can lead to covalent interactions with TMC, improving the crosslinking degree and creating multiple growth directions, resulting in extensive fishnet-like structures [41]. Similarly, crumpled surface morphology was reported in studies incorporating modified MoS$_2$ (TA-MoS$_2$) nanosheets, and the change was related to the promoted IP reaction and participation of functional groups attached to the nanosheets [31]. It is noteworthy that the OH–MoS$_2$ nanosheet exhibited no aggregation and unselective defect

Fig. 3 ATR-FTIR spectra of control PPA and OH–MoS$_2$ PPA membranes
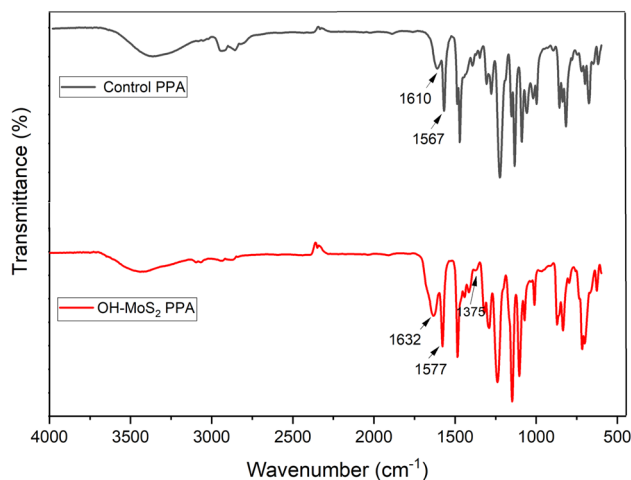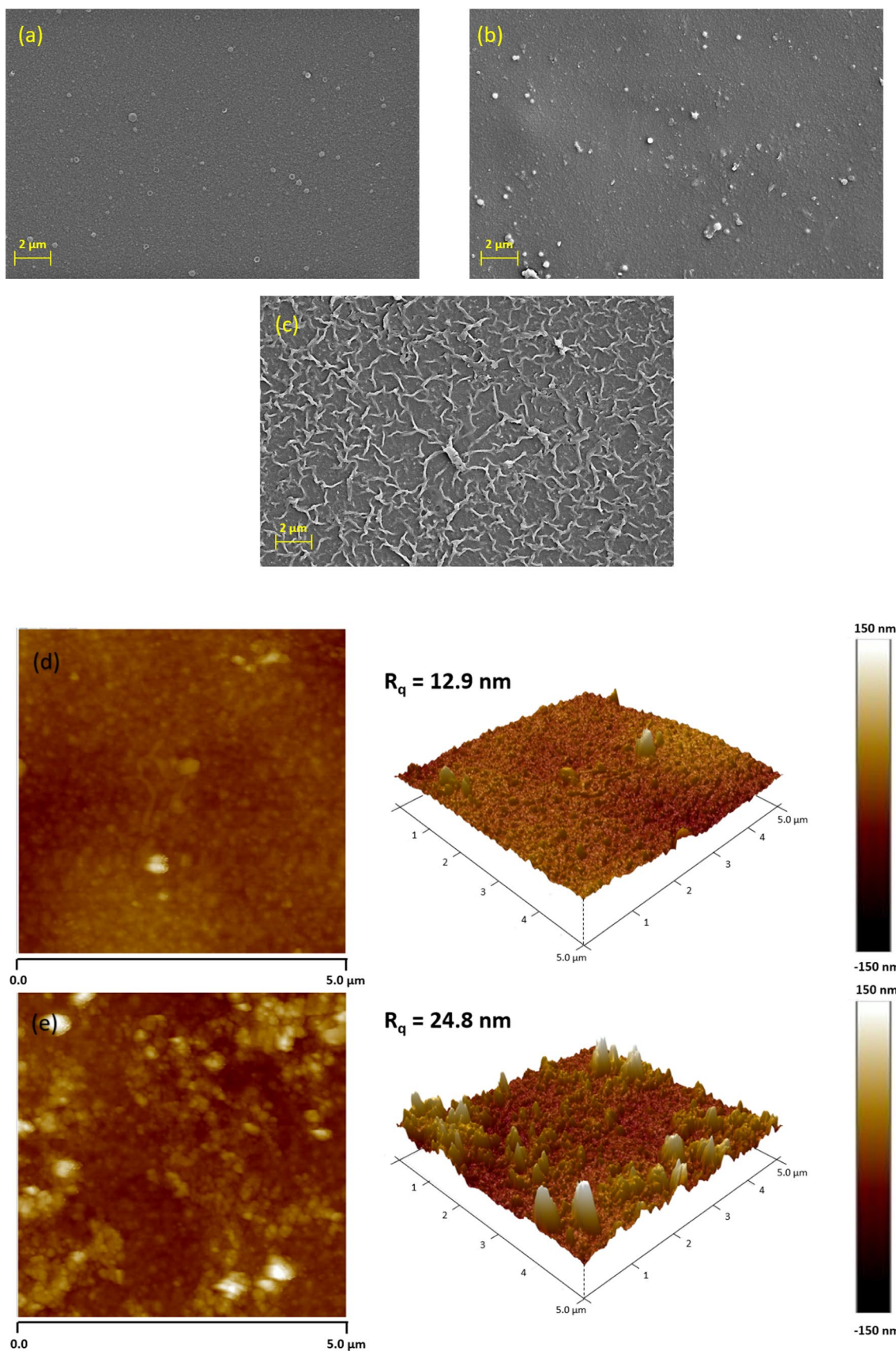
Fig. 4 SEM surface morphologies of **a** XN 45, **b** control PPA and **c** OH–MoS$_2$ PPA membrane, 2D and 3D AFM images of **d** control PPA and **e** OH–MoS$_2$ PPA membrane

formation owing to the improved compatibility with the polymer matrix facilitated by OH functionalization of the nanosheets. Further the SEM cross-sectional image analysis revealed noteworthy differences in the average thickness of the selective polyamide layer between the control PPA and OH–MoS$_2$ PPA membranes. The control PPA membrane exhibited an average thickness of 130 nm, while the OH–MoS$_2$ PPA membrane displayed a slightly thicker PPA layer, measuring 206 nm. The promoted IP reaction along with the orientation of nanosheets in the vertically and multiple polymer growth directions resulted in increasing the thickness of the selective polyamide layer for the OH–MoS$_2$ PPA membrane as shown in Additional file 1: Figure S3 (a-b). Despite the increased PPA layer thickness in the MoS$_2$ PPA membrane, the interfacial voids and crumpled structure within the membrane surface enhanced the membrane permeance [19, 26].

AFM analysis of the membrane surface deciphered the impact of incorporating OH–MoS$_2$ nanosheets into the PA layer. The 2D and 3D AFM images with a scan area of 5 µm × 5 µm for the control PPA and OH–MoS$_2$ PPA are shown in Fig. 4d, e. As shown in Fig. 4d, the control PPA membrane consists of several peaks due to bubble-like nodular structure of the PPA film, as supported through SEM analysis. The surface roughness values of the membranes are listed in Table 1. The control PPA membrane exhibited a smoother surface with R_q value of 12.9 nm, while the XN 45 membrane showed moderate R_q value of 18.6 nm (Fig. 4d and Additional file 1: Figure S4). Incorporation of OH–MoS$_2$ nanosheet remarkably increased the roughness R_q value to 24.9 nm due to the formation of crumpled fishnet-line structures, which is in agreement with the SEM observations in Fig. 4c. In general, a rougher membrane surface facilitates increased surface area available for filtration, which enhances membrane permeance. This leads to the formation of a water hydration layer over the membrane surface, boosting its antifouling performance [42]. The increased surface roughness was attributed to the interaction of OH–MoS$_2$ nanosheets during the IP reaction, leading to a local enrichment of PIP molecules in the organic phase, improving the reaction kinetics, and facilitating multiple growth directions with visible fishnet-like protuberances [31].

The hydrophilicity of the membranes was measured using CA analysis. Hydrophilic surface is linked with lower CA, which enhances membrane wettability and improves the fouling resistance of the membrane [43]. A hydrophilic surface prevents the deposition of NOM onto the membrane and facilitates higher removal of NOM due to the formation of water hydration layer [5]. Therefore, engineering membrane surface hydrophilicity and roughness is key to developing organic fouling-resistant NF membranes [7]. The roughness data and CA measurements are tabulated in Table 1. The OH–MoS$_2$ PPA membrane with a CA of 29.20° exhibited hydrophilic surface than the control PPA and XN 45 membrane with a CA of 43° and 39°, respectively. This was due to the hydrophilic characteristics of the incorporated 2D OH–MoS$_2$ nanosheets and the ability of the hydroxyl groups of the nanosheets to absorb water molecules via hydrogen bonding [32]. Nevertheless, the enhanced hydrophilicity of the membrane surface can act as a double-edged sword during filtration with hydrophilic fractions of NOM [5]. In this study, both hydrophilic and hydrophobic NOM were used to evaluate organic fouling and NOM removal performance. The enhanced membrane hydrophilicity can boost the formation of a water hydration layer, mitigating the deposition of hydrophobic organic surrogates such as HA; however, it can increase the bridging and adsorption of hydrophilic NOM fractions such as SA and bovine serum albumin (BSA), which can aggravate fouling [4]. Therefore, investigating membrane surface hydrophilicity and its interaction with NOM is highly relevant for engineering fouling-resistant membranes.

In addition to membrane surface hydrophilicity, the surface charge also controls the removal of NOM and fouling performance [5]. The surface charge properties of control PPA and OH–MoS$_2$ PPA were evaluated using streaming potential measurements. In general, PPA membranes possess a negative charge at neutral pH due to the disassociation of the free carboxylic groups present in the polymer chain. The IP reaction gives rise to a polyamide structure; however, the residual unreacted acyl chloride groups hydrolyse into carboxylic groups, which deprotonate at pH values higher than their pKa [44]. Membranes with negative surface charges are always preferred for NOM removal, as the NOM moieties possess a negative charge at neutral pH, enhancing their removal and fouling mitigation properties [5]. The electrostatic interactions between NOM and the membrane surface restrict the deposition of organic matter on the membrane surface, thereby alleviating membrane fouling. The OH–MoS$_2$ PPA membrane possesses a negative charge of − 44.45 mV

Table 1 Tabulation of membrane surface properties of membranes tested in this study

Membrane ID	Roughness (R_q in nm)	CA (°)	Streaming potential at pH 7 (mV)
XN 45	18.6 ± 1.81	39 ± 1.24	− 35.46
Control PPA	12.9 ± 1.81	43 ± 1.12	− 28.46
OH–MoS$_2$ PPA	24.9 ± 1.12	29.20 ± 0.86	− 44.45

which is almost 56% higher than the control PPA at − 28.46 mV and 25% higher than XN 45 membrane at 35.46 mV as shown in Table 1. This was due to the electronegative nature of the OH–MoS$_2$ nanosheets on the membrane surface [32]. The hydroxyl groups attached to the nanosheets also increase the negative charge of the membrane [32]. As the NF membrane separation is also dependent on the electrostatic interactions between the solutes and the membrane surface, the enhanced surface negative charge on the incorporation of OH–MoS$_2$ nanosheets could facilitate increased repulsive behaviour towards negatively charged salt ions and NOM molecules, which further improves the selectivity and fouling resistance of the membranes [25].

Filtration performance of NF membranes

Pure water permeance and salt rejection

TFN NF membranes incorporated with 0.010 wt.% OH–MoS$_2$ nanosheets in the aqueous phase during the IP reaction enhanced the pure water permeance by 46.33% from 11.20 to 16.39 L m^{-2} h^{-1} bar^{-1} against the control PPA membrane, as depicted in Fig. 5a. The TFN membrane also exhibited excellent salt rejection performance, bridging the trade-off between enhanced water permeance and rejection. This was mainly attributed to the enhanced electronegative properties of the membrane surface with OH–MoS$_2$ nanosheets [45]. Studies have also reported that partial coverage of membrane pores by MoS$_2$ nanosheets can increase the salt separation properties owing to the additional sieving effect [37]. The TFN membrane exhibited salt rejection (Na$_2$SO$_4$) of 96.3% compared with 90.82% for the control membrane, as shown in Fig. 5b. The TFN membrane incorporated with OH–MoS$_2$ nanosheets showed higher water flux and salt rejection compared with XN 45 NF membrane, which supports its relevance and practical application for surface water treatment. The modified TFN membrane also exhibited tremendous increase in rejection performance for MgSO$_4$ and NaCl at (85.2% → 94.16%) and (36.48% → 70.45%), respectively, compared to the control PPA membrane. This performance enhancement was linked to the OH–MoS$_2$ nanosheets and its ability to engineer membrane surfaces with suitable hydrophilic and electronegative properties. The hydrophilic properties of OH–MoS$_2$ nanosheets could be favourable to form hydrogen bonds with water molecules, facilitating ultrafast transport, and enhancing membrane water permeance [25]. The hydrophilicity and surface charge of the TFN membrane surface increased upon incorporation of the nanosheets, as evidenced by the CA and zeta potential values in Table 1. The surface micromorphology was transformed into rough crumpled fishnet-like structures owing to the interactions of the OH–MoS$_2$ nanosheets during the IP reaction via hydrogen bonding. This leads to the formation of additional selective nanovoids and micropores, which enhance the flux of the membranes [31].

The presence of Mo–O and S=O bonds in the OH–MoS$_2$ nanosheets promotes the IP reaction and enhances the degree of crosslinking of the polymer matrix, improving the selectivity of the membrane [46]. The intrinsic nanopores of OH–MoS$_2$ nanosheets, along with their interfacial and interlayer voids, can also contribute to improving water permeance
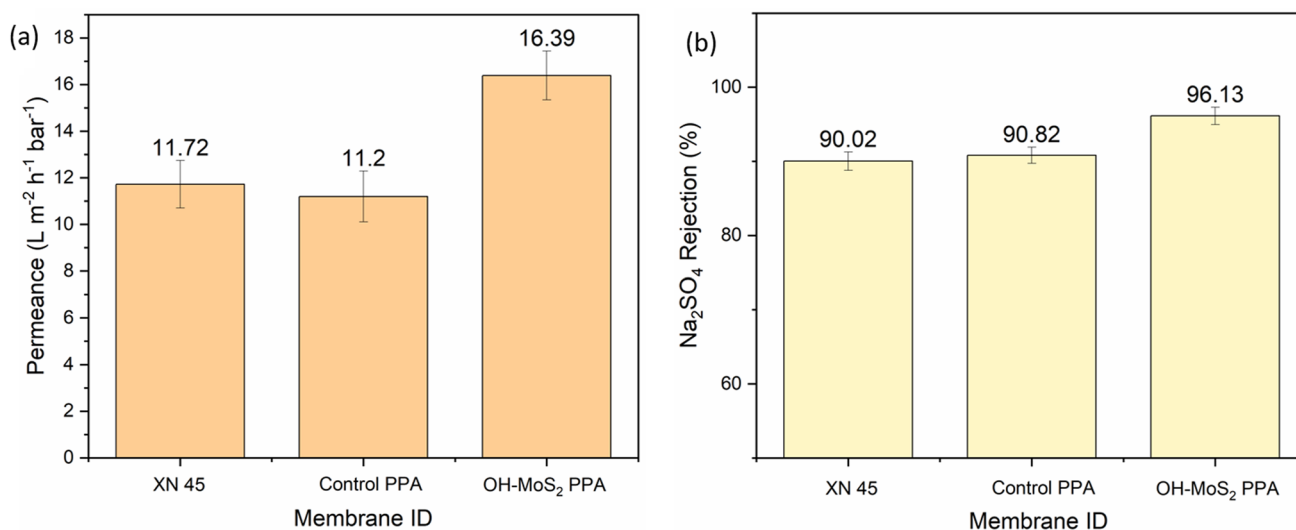
Fig. 5 **a** Pure water permeance and **b** Na$_2$SO$_4$ rejection for the NF membrane evaluated in this study

[32]. Comparison with existing studies on various 2D engineered TFN NF membranes incorporating MoS_2, BN, GO, and g-C_3N_4 indicated that the OH–MoS_2 membrane in this study exhibited superior performance with water permeance and salt rejection at 16.39 L m^{-2} h^{-1} bar^{-1} and 96.3%, respectively, bridging the trade-off between permeance and rejection, as shown in Additional file 1: Table S1. Furthermore, the modified TFN NF membrane in this study had approximately twice the water permeance of previous studies that used MoS_2 for TFN membrane synthesis [24, 25, 46]. This enhanced performance supports a new strategy for engineering membranes with OH–MoS_2 nanosheets for emerging nanofiltration applications.

Fouling resistance performance and NOM removal

Analysis of the fouling experiments and normalized flux profiles showed that the OH–MoS_2 nanosheets-engineered TFN membrane resulted in enhanced fouling resistance and NOM removal for both hydrophobic and hydrophilic NOM fractions. Fouling experiments with the control PPA membrane exhibited normalized fluxes of 89.71% and 74.25% at the conclusion of the 6 h tests for HA and SA NOM fractions, respectively (Fig. 6a–d), while the OH–MoS_2 PPA membrane showed a normalized flux of 95.09% and 93.26%, respectively (Fig. 6e–h). To benchmark the fouling trend, commercial XN 45 membranes were also tested under similar conditions and the normalized flux profiles are include in Additional file 1: Figure S5 (a–d). At the end of 6 h fouling experiments, the normalized flux was at 88.79% and 78.54% for HA and SA feed solutions, respectively. The commercial XN 45 membrane showed rejection of 83.64% and 91.06% for HA and SA in terms DOC, respectively, as shown in Fig. 7a, d. The OH–MoS_2 PPA membrane exhibited enhanced NOM removal at 89.26% and 93.46% for HA and SA feed solutions, respectively, while the control PPA NOM removal was 84.56% and 90.54%, respectively, as shown in Fig. 7c, f and Fig. 7b, e. The improved performance of the OH–MoS_2 PPA membrane can be attributed to its enhanced hydrophilicity, electrostatic repulsion, and modified surface morphology [24]. The higher negative charge properties of the OH–MoS_2 PPA membrane resulted in effective repulsion of NOM molecules. Both HA and SA molecules hold a negative charge under neutral pH maintained for the feed solution, which enhances the repulsion between NOM and the negatively charged membrane surface [5]. The increased surface roughness and hydrophilicity of the membrane, as evidenced through AFM and CA analysis, can support the formation of a water hydration layer reducing the attachment of NOM to the membrane, improving both the antifouling and NOM removal performance [47]. The literature also suggests that a super-hydrophilic membrane surface can worsen fouling owing to its interactions and the deposition of hydrophilic NOM fractions [5]. However, the OH–MoS_2 PPA membrane performed well and exhibited excellent performance when handling both the SA and HA feed solutions, establishing its operational versatility in handling both the hydrophobic and hydrophilic fractions of NOM. This can be attributed mainly to the electrostatic repulsive separation mechanism of NOM, which prevents the deposition of SA on the membrane surface [48].
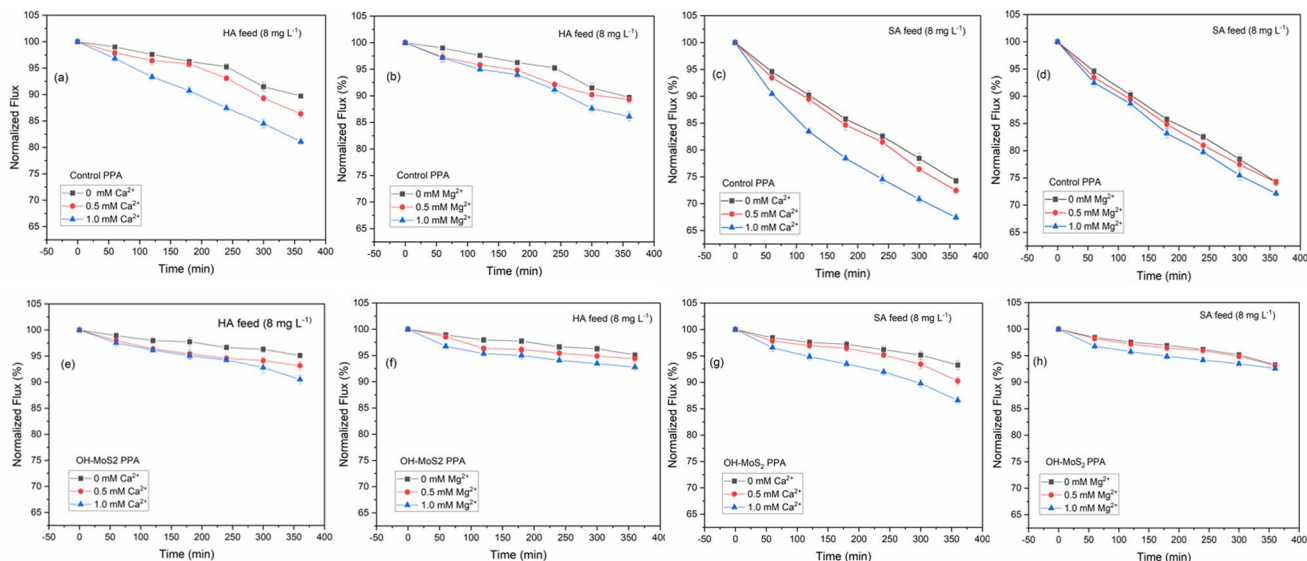
Fig. 6 Trends of normalized flux during 6 h fouling tests conducted under different divalent cation contents and NOM feed solutions for the control PPA (**a–d**) and OH–MoS_2 PPA (**e–h**)
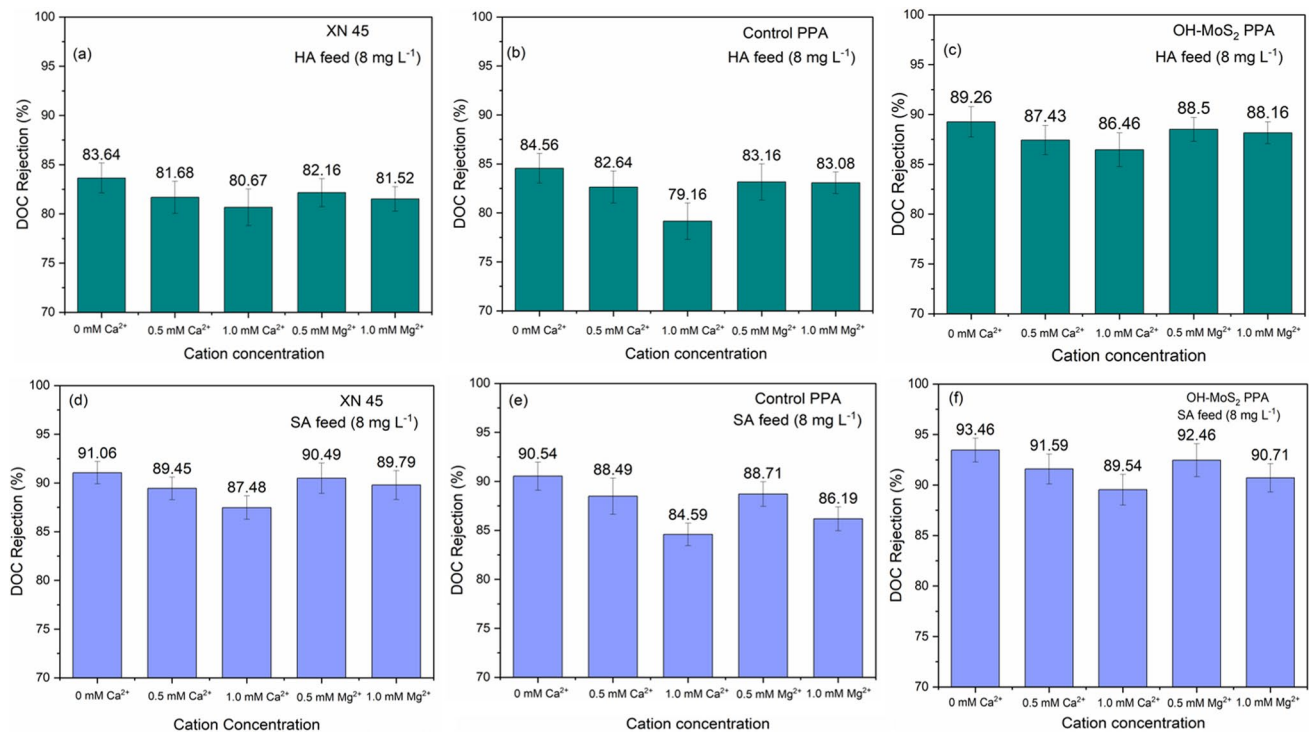
Fig. 7 NOM rejection in terms of DOC during filtration studies with HA feed solution for **a** XN45, **b** control PPA, and **c** OH–MoS$_2$ PPA, and with SA feed solution for **d** XN45, **e** control PPA, and **f** OH–MoS$_2$ PPA

Notably, the OH–MoS$_2$ PPA membrane exhibited better performance than the commercial XN 45 membrane in terms of NOM removal and normalized flux under similar filtration conditions, as shown in Additional file 1: Table S2. In addition to membrane properties such as hydrophilic and electrostatic interactions, membrane surface roughness significantly impacts the fouling behaviour of NF membranes [7]. The enhanced organic fouling and removal performance of OH–MoS$_2$ PPA could also be attributed to the increased surface roughness on incorporation of the nanosheet. Heightened surface roughness amplifies the available filtration area and facilitates the creation of a hydration layer on the membrane's surface which pushes away the organic molecules reducing their deposition while improving the water permeance and organic removal. Similar property to performance relationship between increased roughness and improved fouling performance has been reported for nanomaterial-engineered TFN membranes [5, 49]. While increased surface roughness can enhance water permeance and organic fouling resistance, it introduces a significant concern related to fouling entrapment. The intricate ridge and valley structure of rough membranes can trap organic foulants, leading to the severe organic fouling [7]. However, the increased hydrophilicity, negative charge, and surface roughness together improved the fouling performance for the OH–MoS$_2$ PPA membrane.

The antifouling performance of the 0.010 wt.% OH–MoS$_2$-enabled NF membrane was critically compared with other 2D nanosheets-enabled TFN membranes, and the results are summarized in Table 2. Among these studies,

Table 2 Comparison of NOM fouling behaviour of OH–MoS$_2$-incorporated membrane with functionalized MoS$_2$ and other 2D nanosheet-engineered TFN membrane

2D nanosheet	Fouling agent	Filtration conditions	Normalized flux (%)	References
OH–MoS$_2$	HA	6 bar, 360 min	95.09	This work
OH–MoS$_2$	SA	6 bar, 360 min	93.26	This work
S-MoS$_2$	BSA	4 bar, 60 min	91	[24]
O-MoS$_2$	BSA	3.5 bar, 90 min	78	[25]
TA-MoS$_2$	BSA	6 bar, 240 min	60	[29]
BN(NH$_2$)	SA	6 bar, 360 min	95	[37]
MXene	BSA	16 bar, 360 min	89.9	[47]

OH–MoS$_2$-incorporated TFN membrane outperformed other TFN membranes, establishing its superior fouling mitigation properties for handling both the hydrophobic and hydrophilic fractions of NOM. The higher water permeance, enhanced salt rejection, and NOM removal performance, as summarized in Additional file 1: Tables S1 and S2, support the application of the OH–MoS$_2$ TFN membrane for surface water treatment while exhibiting excellent fouling mitigation and NOM removal performance.

Impact of Ca^{2+} and Mg^{2+} on NOM fouling and removal performance

The NOM feed solution containing HA and SA (pH maintained at 7) was spiked with Ca^{2+} and Mg^{2+} (0, 0.5, and 1.0 mM) to evaluate the effects of divalent cations on NOM fouling and removal. Figure 6a–h shows the normalized flux trend of the NF membranes during the 6 h fouling experiments. All membranes employed in this study exhibited flux decline due to membrane fouling, and the presence of Ca^{2+} and Mg^{2+} worsened fouling and reduced NOM removal performance.

In the case of the HA feed solution, an increase in the Ca^{2+} concentration from 0 to 1.0 mM led to a significant decline in the normalized flux from 89.71 to 81.08% for the control PPA membrane (Fig. 6a), while the normalized flux declined from 88.79 to 80.38% for the commercial XN 45 membrane (Additional file 1: Figure S5 (a)). The OH–MoS$_2$ PPA membrane still performed better than the control PPA and XN 45 membrane, with a decline in the normalized flux from 95.09 to 90.52% owing to its enhanced membrane surface properties. When the concentration of Mg^{2+} was increased from 0 to 1.0 mM, the normalized flux decreased to 86.11% and 84.74% for control PPA (Fig. 6b) and XN 45 membrane (Additional file 1: Figure S5 (b)), respectively, while it was maintained at 92.79% for OH–MoS$_2$ PPA membrane. The NOM removal performances of the control PPA and OH–MoS$_2$ PPA membranes are shown in Fig. 7a–c and benchmarked against the commercial XN 45 membrane. In the absence of cations, the DOC rejection of the membranes was 83.64%, 84.56%, and 89.26% for the XN 45, control PPA, and OH–MoS$_2$ PPA membranes, respectively. At 1 mM concentration of Ca^{2+} ions in the feed, the DOC rejection decreased to 80.67%, 79.16%, and 86.46%, respectively, for XN 45, control PPA, and OH–MoS$_2$ PPA membranes. The modified membrane exhibited excellent performance in retaining NOM rejection at detrimental Ca^{2+} levels. The DOC rejection values for XN 45, control PPA, and OH–MoS$_2$ PPA membranes in the presence of 1.0 mM Mg^{2+} were at 81.52%, 83.08%, and 88.16, respectively. Ca^{2+} and Mg^{2+} significantly impact the HA properties owing to their interactions through electrostatic charge effects and complex formation and facilitate the formation of chemical bridges between HA and polymer matrix of the membrane surface [50]. Ca^{2+} and Mg^{2+} facilitated the attachment of HA to membrane surface owing to decreased interchain electrostatic repulsion between HA, and between the HA and polyamide layers [51]. Compared to Mg^{2+}, Ca^{2+} exacerbated fouling and NOM removal, which could be attributed to its greater charge neutralization capability and favourable ability to attach to HA molecules [52]. This could lead to the formation of colloidal aggregates of HA with a lower zeta potential, owing to the neutralization of the negative charge caused by the favourable specific charge and complexation ability of cations. The lower impact of Mg^{2+} ions on HA fouling could also be linked to the high affinity of Mg^{2+} ions for water molecules and its strongly held hydration shell, which weakens its interaction with HA compared with Ca^{2+} [53]. In contrast to many studies reporting a higher fouling impact of HA foulants in the presence of Ca^{2+}, studies have also reported a superior charge screening effect and charge density of Mg^{2+} to cause more severe fouling compared to Ca^{2+} [3, 54]. However, cation interactions with NOM and associated fouling are highly dependent on NOM content, feed water chemistry, membrane surface properties, and operating parameters of nanofiltration [5].

In addition, the presence of cations such as Ca^{2+} and Mg^{2+} in natural water promotes the formation of DBPs during the disinfection process [55, 56]. Interestingly, studies have indicated that DBP formation tends to be more pronounced in the presence of Ca^{2+} when compared to Mg^{2+} [57]. This phenomenon can be attributed to the binding of these cations to the carboxylate groups within NOM molecules, forming metal carboxylate complexes that facilitate DBP formation. The higher Lewis acidity of Mg^{2+}, relative to Ca^{2+}, has been identified as a key influencing parameter that enhances DBP formation. Notably, various NOM fractions, including polyols, citric acid, and humic acid, have shown an increased propensity for DBP formation in the presence of cations, as compared to substances such as resorcinol, histidine, and dicarboxylic acids [55, 57].

Figure 8a–c shows the microstructures of the air-dried droplets of the HA solution viewed under a microscope. It is evident that in the presence of 1 mM Ca^{2+} and Mg^{2+}, HA molecules tend to aggregate, with Ca^{2+} causing the formation of larger aggregates. This behaviour can be linked to the neutralization of the negative charge of HA in the presence of cations, which facilitates the formation of aggregates. With increasing cation content, the negative charge of the feed solution decreased, and Ca^{2+} ions exhibited a more powerful ability to neutralize the negative charge owing to the strong affinity for carboxylic groups, as observed in Additional file 1: Table S3. SEM images of the fouled membranes after 6 h
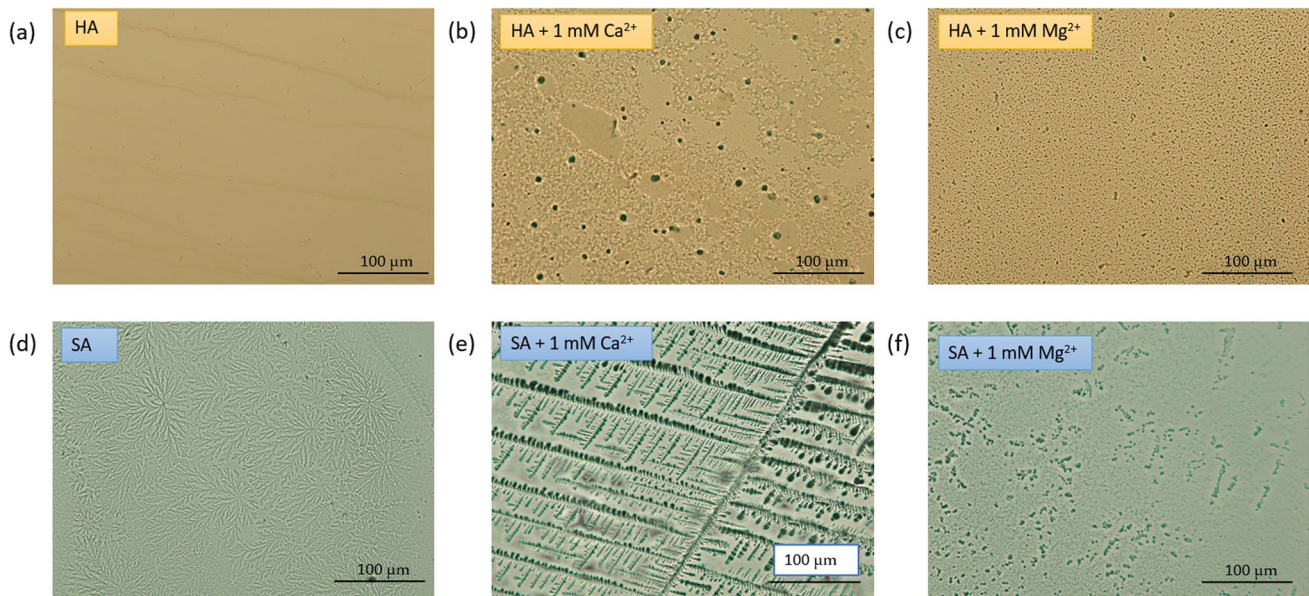
Fig. 8 Microscopic images showing microstructures of the air-dried droplets of **a** HA solution, **b** HA + 1 mM Ca^{2+}, **c** HA + 1 mM Mg^{2+}, **d** SA solution, **e** SA + 1 mM Ca^{2+}, **f** SA + 1 mM Mg^{2+} (Feed concentration of HA and SA solution was maintained at 8 mg L^{-1})

of fouling experiments were compared to understand HA fouling deposition on the membrane surface. Figure 9a–c shows the fouled control PPA membranes with 0 and 1 mM Mg^{2+} and 1 mM Ca^{2+}, respectively. It can be observed that the intensity of foulant deposition increases in the presence of cations, causing a decline in flux, as reported in this study. This was mainly attributed to the reduced electrostatic repulsion between the membrane surface and HA molecules with divalent cations, facilitating its attachment on the membrane surface. The formation of large unstable HA colloidal aggregates causes pore blockage within the membrane pores, which causes significant fouling and flux decline [52]. The SEM image of fouled XN 45 membrane with HA + 1 mM Ca^{2+} as shown in Additional file 1: Figure S6 (a) also showcased significant foulant deposition. In contrast, our OH–MoS$_2$ PPA membrane exhibited improved resistance to fouling compared to the commercial XN 45 membrane. The OH–MoS$_2$ PPA membrane with its enhanced surface charge and hydrophilic properties lowered the deposition of hydrophobic HA compared to that of the control PPA and XN 45 membrane, as shown in Fig. 9d–e. The modified membrane's improved hydrophilicity and surface roughness may make it easier for a water hydration layer, reducing the deposition of unstable NOM aggregates [58]. The higher electronegative charge of the engineered membrane compared to the control PPA can repel HA molecules, reducing foulant deposition [20]. Flux recoverability tests revealed that the OH–MoS$_2$ PPA membrane exhibited a high relative flux recovery ratio (FRA) during filtration and cleaning tests with the HA feed, as shown in Additional file 1: Table S4. The control PPA membrane exhibited a declining trend in FRA at 92.25%, 81.54%, and 88.46% for HA, HA + 1 mM Ca^{2+}, and HA + 1 mM Mg^{2+}, respectively. This shows that at high Ca^{2+} levels, membrane fouling recoverability decreases because of the deposition of foulants with strong bridging between Ca^{2+}, HA, and the membrane surface [59–61]. Owing to its enhanced surface properties, OH–MoS$_2$ PPA membrane exhibited superior and stable FRA > 95% during all the fouling cleaning trials with varying cation content in the feed water.

Filtration tests with the SA solution exhibited worse fouling than HA. SA is a typical polysaccharide fraction of NOM that exhibits a high fouling propensity, which could be attributed to the gelling tendency of SA and its ability to form a dense fouling layer, causing a steep flux decline [62]. The normalized flux of the control PPA membrane decreased to 72.45% and 67.46% from 74.25% for feed water containing 0.5 and 1.0 mM of Ca^{2+}, respectively, while OH–MoS$_2$ PPA membrane retained excellent performance with normalized flux of 90.25% and 86.58% from 93.26%, respectively, as shown in Fig. 6d, h. In the case of XN 45 membrane addition of 1.0 mM of Ca^{2+} to the SA solution reduced the normalized flux from 78.54 to 70.16% as shown in Additional file 1: Figure S5 (c). The SA feed solution with 1 mM Mg^{2+} led to a slight decline in the normalized flux to 72.16% and 74.51% for the control PPA and XN 45 (Additional file 1: Figure S5 (d)) membrane, respectively, whereas the OH–MoS$_2$ PPA membrane exhibited a negligible decline in the normalized flux to 92.58%. NOM rejection in terms of DOC also showed a decreasing trend with increasing Ca^{2+} and Mg^{2+}. At 1 a concentration of Ca^{2+}, the DOC rejection decreased from 90.54 to 84.59%, whereas at similar concentrations of Mg^{2+}, DOC rejection
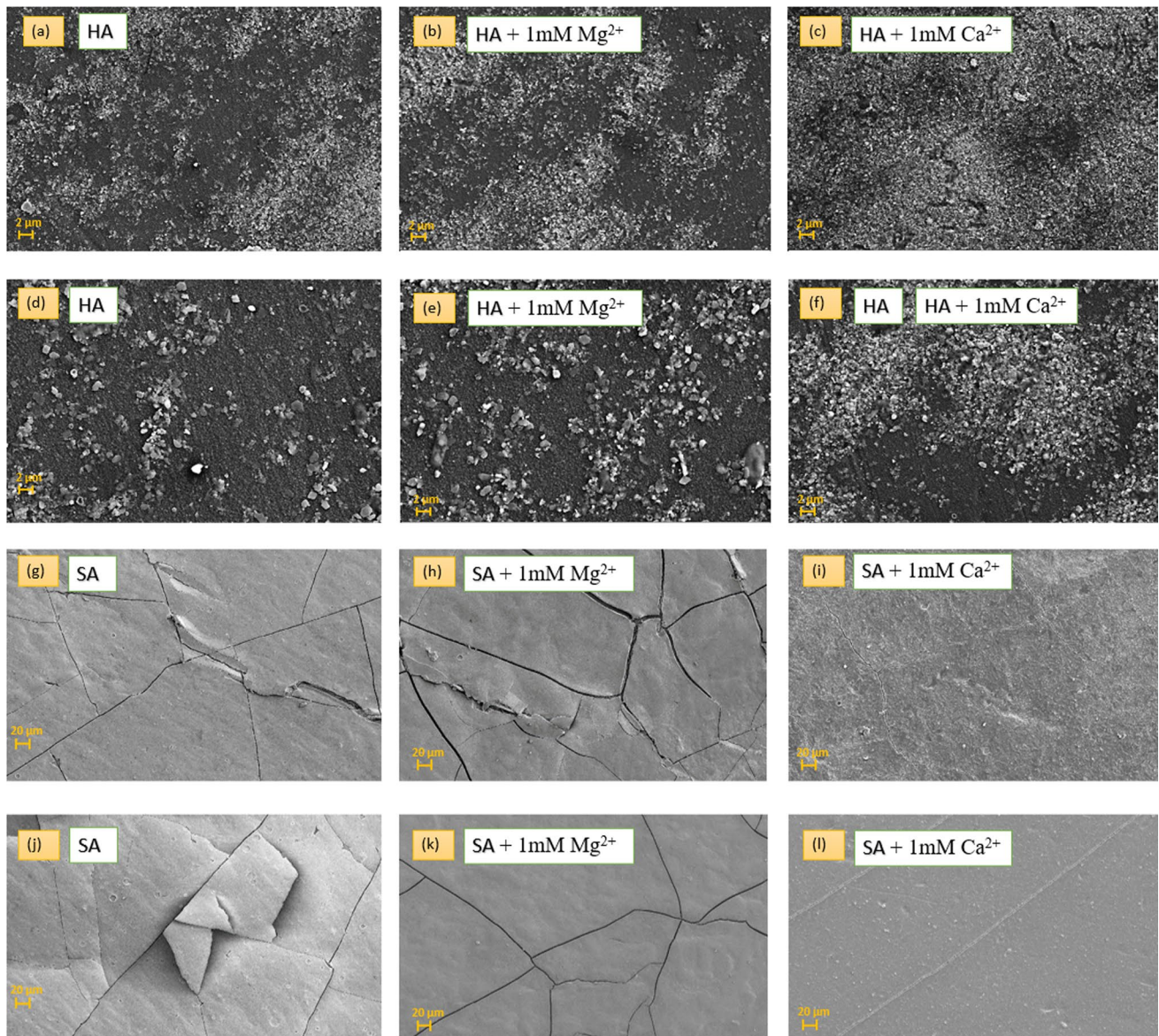
Fig. 9 SEM images of fouled control PPA membrane with **a** HA, **b** HA + 1 mM Mg^{2+}, **c** HA + 1 mM Ca^{2+}, OH–MoS_2 PPA membrane fouled with **d** HA, **e** HA + 1 mM Mg^{2+}, **f** HA + 1 mM Ca^{2+}, control PPA membrane with **g** SA, **h** SA + 1 mM Mg^{2+}, **i** SA + 1 mM Ca^{2+}, and OH–MoS_2 membrane fouled with **j** SA, **k** SA + 1 mM Mg^{2+}, **l** SA + 1 mM Ca^{2+}

decreased to 86.19% for control PPA membrane. OH–MoS_2 PPA membrane maintained stable DOC rejection > 89% under varying cation concentrations, exhibiting its enhanced NOM removal performance.

Figure 9g–l shows the SEM images of fouled control PPA and OH–MoS_2 PPA membranes tested with SA solution adding 0, 1 mM Mg^{2+} and 1 mM Ca^{2+}, respectively. Increasing the Ca^{2+} led to the formation of extensive polysaccharide-crosslinked structures, which significantly increased the deposition of a dense fouling layer on the membrane surface, as depicted in Fig. 9g–l. There is a significant formation of a dense fouling layer caused by the gelling tendency of SA in the presence of Ca^{2+} and Mg^{2+}. According to the Derjaguin–Landau–Verwey–Overbeek (DLVO) theory, the presence of Ca^{2+} leads to the formation of aggregates and destabilizes NOM colloids due to the electrical double layer compression of NOM, decreasing its electrostatic repulsive forces [9]. This led to the formation of SA aggregates in a thick and dense gel layer, as shown in Fig. 9i. Similarly thick and dense fouling layer was observed for XN 45 membrane fouled with SA + 1 mM Ca^{2+} feed solution (Additional file 1: Figure S6 (b)). Studies have also reported that Mg^{2+} has a negative impact on membrane fouling, as Mg^{2+} promotes the crosslinking of alginate molecules increasing its gelling tendency [62, 63]. The higher charge density of Mg^{2+} compared to that of Ca^{2+} could evoke a stronger electrostatic shielding effect,

increasing SA gelling and deposition on the membrane surface. In contrast to Ca^{2+}-induced gels, gelation has been shown to occur at a much greater concentration for Mg^{2+} [62, 64]. It is worth noting that this particular study focused on mimicking the surface water conditions, and hence, at similar concentrations, 1 mM Ca^{2+} induced higher fouling than Mg^{2+}. The SEM images of the fouled control PPA membrane and OH–MoS_2 PPA membrane, as shown in Fig. 9h, k at 1 mM Mg^{2+} concentration, exhibit a more loosely placed gel layer with lower intensity and packing compared to fouling with 1 mM Ca^{2+}, as depicted in Fig. 9i, l.

Figure 8d–f shows the microstructures of the air-dried droplets of the SA solution viewed under a microscope. In the presence of Ca^{2+}, the SA molecules form intensive combined crystal aggregates, which causes dense fouling layer development, as observed in the microscopic image of the NOM droplet (Fig. 8e) and the fouled membrane, as shown in Fig. 9i. Additional file 1: Table S3 also confirms that the zeta potential of the SA solution was lowest in the presence of 1 mM Ca^{2+}. SA has a rigid fibrous structure that forms an intensively crosslinked structure in the presence of Ca^{2+}, significantly worsening fouling and leading to a lower normalized flux. Due to this, the foulant layer was less responsive to water flushing, showing a declining trend for control PPA membrane with FRA at 95.46%, 80.46%, and 85.46% for SA, SA + 1 mM Ca^{2+}, and SA + 1 mM Mg^{2+}, respectively, whereas OH–MoS_2 PPA membrane exhibited excellent performance with FRA > 95%. Owing to the surface charge and hydrophilicity of the OH–MoS_2 nanosheet, the TFN membrane performed well under detrimental levels of Ca^{2+} and Mg^{2+} cations during fouling and NOM removal. Additional file 1: Table S5 summarizes the findings of the current investigation and the literature on the impact of Ca^{2+} and Mg^{2+} ions on the organic fouling of membranes. The presence of cations changes the characteristics of NOM, resulting in severe fouling of the membrane surface. Ca^{2+} induces more intense fouling than Mg^{2+}. For the control PPA membrane, the hydrophilic NOM fraction of SA induced more severe fouling than the hydrophobic NOM fraction of HA did. The OH–MoS_2 nanosheet-engineered NF membrane demonstrated excellent antifouling and NOM removal performance during filtration tests with both hydrophilic and hydrophobic fractions of NOM, as well as at detrimental levels of cations owing to its modified hydrophilicity, negative charge, and membrane surface morphology. As a result, this study demonstrates the operational adaptability of OH–MoS_2-engineered membranes in dealing with NOM and divalent cations during surface water treatment for potable water production.

While our study highlights the promising performance of 2D MoS_2-engineered NF membranes in addressing organic fouling and NOM removal, it is imperative to acknowledge the practical constraints when considering their scale-up for industrial applications. Integrating nanosheet materials into existing membrane manufacturing processes and equipment presents challenges and opportunities, including potential material degradation, leaching, or alterations in surface properties over time, which can impact membrane lifespan and maintenance requirements [5, 19]. For the successful adoption of 2D engineered membranes in the industrial context, a thorough evaluation of operational and financial benefits is essential. Balancing the additional costs associated with nanosheet procurement and integration against the potential benefits in terms of extended membrane lifespan and improved water quality is crucial. Any modification to membrane manufacturing processes must align with environmental standards to ensure the responsible implementation of nanosheet materials, minimizing environmental risks and regulatory concerns. While our study underscores the potential benefits of MoS_2 nanosheets in membrane manufacturing systems, addressing these opportunities is vital for their safe and effective integration into the water treatment industry.

Conclusions

In this study, a TFN membrane was synthesized using OH–MoS_2 nanosheets as the nanofiller (0.010 wt.%) in the aqueous monomer phase to engineer fouling-resistant membranes to handle the NOM issue. The engineered TFN membrane exhibited enhanced hydrophilicity, negative charge, and rougher membrane surface, which increased the membrane water permeance by 46.33% from 11.2 to 16.39 L m^{-2} h^{-1} bar^{-1} when compared to the control PPA membrane, while a very high salt rejection was retained at 96.3% for Na_2SO_4. During 6 h of filtration trials with both hydrophobic (HA) and hydrophilic (SA) fractions of NOM, the modified membrane demonstrated improved fouling resistance and NOM removal. Normalized fluxes of 95.09% and 93.26% were retained with feed water containing HA and SA, respectively. Compared to HA, SA caused more intensive fouling and flux decline in the control PPA membrane, reaching 89.71% and 74.25%, respectively. This performance was linked to the deposition of SA through hydrophilic interactions with the membrane surface. Fouling phenomena are quite complex depending upon NOM properties, its concentration and feed chemistry, and physicochemical properties of the membrane, and filtration conditions. However, engineering TFN membranes with OH–MoS_2 endowed the membrane with favourable surface hydrophilicity, charge, and morphology,

facilitating an enhanced fouling mitigation performance for both HA and SA. This study investigated the impact of Ca^{2+} and Mg^{2+} on the organic fouling and separation performance of membranes. Ca^{2+} had a more detrimental impact on organic fouling and NOM removal than Mg^{2+} for both HA and SA fractions because of its stronger affinity to neutralize and aggregate NOM molecules, as well as form complex bridging with deprotonated groups of NOM and the polymer structure of membrane, causing formation of dense foulant layer on the membrane surface. The TFN membrane outperformed the commercial and control PPA membranes during fouling tests in the presence of 1 mM Ca^{2+} and Mg^{2+} in the feed solution. Owing to the versatile performance of TFN membranes while handling various fractions of NOM and detrimental levels of alkaline earth cations, $OH–MoS_2$-incorporated membranes could be favourable for the treatment of surface water containing NOM to produce potable water.

Data availability Available upon request.

Declarations

Competing interests The authors declare that they have no known competing financial interests or personal relationships that could have influenced the work reported in this study.

Ethics approval and consent to participate Not applicable.

Consent for publication Not applicable.

References

1. Cheng X, Lai C, Zhu X, Shao S, Xu J, Zhang F, et al. Tailored ultra-low pressure nanofiltration membranes for advanced drinking water treatment. Desalination. 2023;548: 116264.
2. Yaqoob AA, Kanwal A, Ibrahim MNM, Mohammad SAG, Ahmad A. Chapter 15—application and fabrication of nanofiltration membrane for separation of metal ions from wastewater. In: Ahmad A, Kumar R, Jawaid M, editors. Emerging techniques for treatment of toxic metals from wastewater. Amsterdam: Elsevier; 2023. p. 365–98.
3. Song Y, Li X, Li C, Li J, Dong Z, Zhang M, et al. Exploring and comparing the roles of Ca^{2+} and Mg^{2+} in small-sized natural organics-induced charged nanofiltration membrane fouling. Sep Purif Technol. 2020;251: 117415.
4. Abdikheibari S, Lei W, Dumée LF, Milne N, Baskaran K. Thin film nanocomposite nanofiltration membranes from amine functionalized-boron nitride/polypiperazine amide with enhanced flux and fouling resistance. J Mater Chem A. 2018;6(25):12066–81.
5. Mallya DS, Abdikheibari S, Dumée LF, Muthukumaran S, Lei W, Baskaran K. Removal of natural organic matter from surface water sources by nanofiltration and surface engineering membranes for fouling mitigation. Chemosphere. 2023;321: 138070.
6. Peters CD, Rantissi T, Gitis V, Hankins NP. Retention of natural organic matter by ultrafiltration and the mitigation of membrane fouling through pre-treatment, membrane enhancement, and cleaning—a review. J Water Process Eng. 2021;44: 102374.
7. Zhao S, Liao Z, Fane A, Li J, Tang C, Zheng C, et al. Engineering antifouling reverse osmosis membranes: a review. Desalination. 2021;499: 114857.

8. Chaukura N, Marais SS, Moyo W, Mbali N, Thakalekoala LC, Ingwani T, et al. Contemporary issues on the occurrence and removal of disinfection byproducts in drinking water-a review. J Environ Chem Eng. 2020;8:103659.

9. Abdikheibari S, Dumée LF, Jegatheesan V, Mustafa Z, Le-Clech P, Lei W, et al. Natural organic matter removal and fouling resistance properties of a boron nitride nanosheet-functionalized thin film nanocomposite membrane and its impact on permeate chlorine demand. J Water Process Eng. 2020;34: 101160.

10. Tian L, Zhou P, Su Z, Liu T, Graham N, Bond T, et al. Insights into the properties of surface waters and their associated nanofiltration membrane fouling: the importance of biopolymers and high molecular weight humics. Chem Eng J. 2023;451: 138682.

11. Banyikwa AT. Evaluation of hydrogeochemical characteristics, spatial distribution of major ions, and water quality for drinking and irrigation in six districts of the Dodoma region in Tanzania. Groundw Sustain Dev. 2023;21: 100897.

12. You X, Teng J, Chen Y, Long Y, Yu G, Shen L, et al. New insights into membrane fouling by alginate: Impacts of ionic strength in presence of calcium ions. Chemosphere. 2020;246: 125801.

13. Shim J, Park S, Cho KH. Deep learning model for simulating influence of natural organic matter in nanofiltration. Water Res. 2021;197: 117070.

14. Shan L, Fan H, Guo H, Ji S, Zhang G. Natural organic matter fouling behaviors on superwetting nanofiltration membranes. Water Res. 2016;93:121–32.

15. Mustafa G, Wyns K, Buekenhoudt A, Meynen V. New insights into the fouling mechanism of dissolved organic matter applying nanofiltration membranes with a variety of surface chemistries. Water Res. 2016;93:195–204.

16. Meng F, Zhang S, Oh Y, Zhou Z, Shin H-S, Chae S-R. Fouling in membrane bioreactors: an updated review. Water Res. 2017;114:151–80.

17. Li D, Lin W, Shao R, Shen Y-X, Zhu X, Huang X. Interaction between humic acid and silica in reverse osmosis membrane fouling process: a spectroscopic and molecular dynamics insight. Water Res. 2021;206: 117773.

18. Adusei-Gyamfi J, Ouddane B, Rietveld L, Cornard J-P, Criquet J. Natural organic matter-cations complexation and its impact on water treatment: a critical review. Water Res. 2019;160:130–47.

19. Mallya DS, Dumee LF, Muthukumaran S, Lei WW, Baskaran K. 2D nanosheet enabled thin film nanocomposite membranes for freshwater production—a review. Mater Adv. 2021;2(11):3519–37.

20. Mansourpanah Y. MXenes and other 2D nanosheets for modification of polyamide thin film nanocomposite membranes for desalination. Sep Purif Technol. 2022;289: 120777.

21. Liu Y, Zhao Y, Zhang X, Huang X, Liao W, Zhao Y. MoS_2-based membranes in water treatment and purification. Chem Eng J. 2021;422: 130082.

22. Xu Y, Zhang W, Li Z, Shen L, Li R, Zhang M, et al. Enhanced water permeability in nanofiltration membranes using 3D accordion-like MXene particles with random orientation of 2D nanochannels. J Mater Chem A. 2022;10(31):16430–8.

23. Deng Y, Zhang J, Li Q, Liu T, Yang Y. A highly chlorine-oxidation and fouling resistant thin film nanocomposite membrane enhanced by few-layered graphitic carbon nitride nanosheets. Environ Sci Water Res Technol. 2022;8(9):1976–91.

24. Zhu J, Meng W, Xue Q, Zhang K. Two dimensional sulfonated molybdenum disulfide (S–MoS_2) thin-film nanocomposite nanofiltration membrane for selective desalination. J Membr Sci. 2023;676: 121574.

25. Yang S, Jiang Q, Zhang K. Few-layers 2D O-MoS_2 TFN nanofiltration membranes for future desalination. J Membr Sci. 2020;604: 118052.

26. Mallya DS, Yang G, Lei W, Muthukumaran S, Baskaran K. Functionalized MoS_2 nanosheets enabled nanofiltration membrane with enhanced permeance and fouling resistance. Environ Technol Innov. 2022;27:102719.

27. Karki S, Gohain MB, Yadav D, Thakare NR, Pawar RR, Hazarika S, et al. Building rapid water transport channels within thin-film nanocomposite membranes based on 2D mesoporous nanosheets. Desalination. 2023;547: 116222.

28. Subrahmanya TM, Lin J-Y, Widakdo J, Austria HFM, Owen S, Chiao Y-H, et al. Effect of functionalized nanodiamonds and surfactants mediation on the nanofiltration performance of polyamide thin-film nanocomposite membranes. Desalination. 2023;555: 116540.

29. Ma M-Q, Zhang C, Zhu C-Y, Huang S, Yang J, Xu Z-K. Nanocomposite membranes embedded with functionalized MoS_2 nanosheets for enhanced interfacial compatibility and nanofiltration performance. J Membr Sci. 2019;591: 117316.

30. Gu Z, Yu S, Zhu J, Li P, Gao X, Zhang R. Incorporation of lysine-modified UiO-66 for the construction of thin-film nanocomposite nanofiltration membrane with enhanced water flux and salt selectivity. Desalination. 2020;493: 114661.

31. Zhang H, Gong X-Y, Li W-X, Ma X-H, Tang CY, Xu Z-L. Thin-film nanocomposite membranes containing tannic acid-Fe^{3+} modified MoS_2 nanosheets with enhanced nanofiltration performance. J Membr Sci. 2020;616:118605.

32. Su Y, Liu D, Yang G, Han Q, Qian Y, Liu Y, et al. Transition metal dichalcogenide (TMD) membranes with ultrasmall nanosheets for ultrafast molecule separation. ACS Appl Mater Interfaces. 2020;12(40):45453–9.

33. Kumar R, Kamakshi KM, Awasthi K. UV-irradiation assisted functionalization and binding of Pd nanoparticles in polycarbonate membranes for hydrogen separation. Environ Sci Pollut Res. 2021;28(34):46404–13.

34. Sohrabi H, Majidi MR, Asadpour-Zeynali K, Khataee A, Dastborhan M, Mokhtarzadeh A. A PCR-free genosensing platform for detection of Shigella dysenteriae in human plasma samples by porous and honeycomb-like biochar decorated with ultrathin flower-like MoS_2 nanosheets incorporated with Au nanoparticles. Chemosphere. 2022;288: 132531.

35. Chaudhary N, Khanuja M, Abid ISS. Hydrothermal synthesis of MoS_2 nanosheets for multiple wavelength optical sensing applications. Sens Actuators A Phys. 2018;277:190–8.

36. Raza A, Ikram M, Aqeel M, Imran M, Ul-Hamid A, Riaz KN, et al. Enhanced industrial dye degradation using Co doped in chemically exfoliated MoS_2 nanosheets. Appl Nanosci. 2020;10(5):1535–44.

37. Abdikheibari S, Lei W, Dumée LF, Barlow AJ, Baskaran K. Novel thin film nanocomposite membranes decorated with few-layered boron nitride nanosheets for simultaneously enhanced water flux and organic fouling resistance. Appl Surf Sci. 2019;488:565–77.

38. Wu Q, Zhang S, Zuo X, Liu L, Xiong J, He J, et al. Preparation and characterization of CeO_2@high silica ZSM-5 inorganic-organic hybrid polyamide nanofiltration membrane. J Membr Sci. 2022;641: 119887.

39. An Q, Li F, Ji Y, Chen H. Influence of polyvinyl alcohol on the surface morphology, separation and anti-fouling performance of the composite polyamide nanofiltration membranes. J Membr Sci. 2011;367(1):158–65.

40. Zhang Y, Ruan H, Guo C, Liao J, Shen J, Gao C. Thin-film nanocomposite reverse osmosis membranes with enhanced antibacterial resistance by incorporating p-aminophenol-modified graphene oxide. Sep Purif Technol. 2020;234: 116017.

41. Xie F, Li W-X, Gong X-Y, Taymazov D, Ding H-Z, Zhang H, et al. MoS$_2$ @PDA thin-film nanocomposite nanofiltration membrane for simultaneously improved permeability and selectivity. J Environ Chem Eng. 2022;10(3): 107697.

42. Xia S, Yao L, Zhao Y, Li N, Zheng Y. Preparation of graphene oxide modified polyamide thin film composite membranes with improved hydrophilicity for natural organic matter removal. Chem Eng J. 2015;280:720–7.

43. Kang Y, Obaid M, Jang J, Kim IS. Sulfonated graphene oxide incorporated thin film nanocomposite nanofiltration membrane to enhance permeation and antifouling properties. Desalination. 2019;470: 114125.

44. Li P, Lan H, Chen K, Ma X, Wei B, Wang M, et al. Novel high-flux positively charged aliphatic polyamide nanofiltration membrane for selective removal of heavy metals. Sep Purif Technol. 2022;280: 119949.

45. Li Y, Yang S, Zhang K, Van der Bruggen B. Thin film nanocomposite reverse osmosis membrane modified by two dimensional laminar MoS$_2$ with improved desalination performance and fouling-resistant characteristics. Desalination. 2019;454:48–58.

46. Yang S, Tian H, Hill MR, Zhang K. Effect and regulation mechanism of oxidation degrees on the O-MoS$_2$ structure and separation performance of nanofiltration membrane. J Membr Sci. 2021;635: 119468.

47. Wang X, Li Q, Zhang J, Huang H, Wu S, Yang Y. Novel thin-film reverse osmosis membrane with MXene Ti$_3$C$_2$T$_x$ embedded in polyamide to enhance the water flux, anti-fouling and chlorine resistance for water desalination. J Membr Sci. 2020;603:118036.

48. Mi Y-F, Zhao F-Y, Guo Y-S, Weng X-D, Ye C-C, An Q-F. Constructing zwitterionic surface of nanofiltration membrane for high flux and anti-fouling performance. J Membr Sci. 2017;541:29–38.

49. Tang K, Zhu L, Lan P, Chen Y, Chen Z, Lan Y, et al. Regulating the thickness of nanofiltration membranes for efficient water purification. Nanoscale Adv. 2023;5(18):4770–81.

50. Al-Amoudi AS. Factors affecting natural organic matter (NOM) and scaling fouling in NF membranes: a review. Desalination. 2010;259(1–3):1–10.

51. Ahn W-Y, Kalinichev AG, Clark MM. Effects of background cations on the fouling of polyethersulfone membranes by natural organic matter: experimental and molecular modeling study. J Membr Sci. 2008;309(1):128–40.

52. Wang L-F, He D-Q, Chen W, Yu H-Q. Probing the roles of Ca^{2+} and Mg^{2+} in humic acids-induced ultrafiltration membrane fouling using an integrated approach. Water Res. 2015;81:325–32.

53. Kalinichev A, Kirkpatrick R. Molecular dynamics simulation of cationic complexation with natural organic matter. Eur J Soil Sci. 2007;58(4):909–17.

54. Mahlangu OT, Mamba BB, Verliefde ARD. Effect of multivalent cations on membrane-foulant and foulant-foulant interactions controlling fouling of nanofiltration membranes. Polym Adv Technol. 2020;31(11):2588–600.

55. Zhao Y, Yang H-W, Liu S-T, Tang S, Wang X-M, Xie YF. Effects of metal ions on disinfection byproduct formation during chlorination of natural organic matter and surrogates. Chemosphere. 2016;144:1074–82.

56. Zhou H, Tian L, Ni M, Zhu S, Zhang R, Wang L, et al. Effect of dissolved organic matter and its fractions on disinfection by-products formation upon karst surface water. Chemosphere. 2022;308: 136324.

57. Navalon S, Alvaro M, Garcia H. Ca^{2+} and Mg^{2+} present in hard waters enhance trihalomethane formation. J Hazard Mater. 2009;169(1):901–6.

58. Liu L, Liu Y, Chen X, Feng S, Wan Y, Lu H, et al. A nanofiltration membrane with outstanding antifouling ability: exploring the structure-property-performance relationship. J Membr Sci. 2023;668: 121205.

59. Katsoufidou KS, Sioutopoulos DC, Yiantsios SG, Karabelas AJ. UF membrane fouling by mixtures of humic acids and sodium alginate: fouling mechanisms and reversibility. Desalination. 2010;264(3):220–7.

60. Wang Y, Zheng X, Li D, Tian J, Wu H, Zhang Y. Comparison of membrane fouling induced by protein, polysaccharide and humic acid under sodium and calcium ionic conditions. Desalination. 2023;548: 116236.

61. Lin T, Lu Z, Chen W. Interaction mechanisms of humic acid combined with calcium ions on membrane fouling at different conditions in an ultrafiltration system. Desalination. 2015;357:26–35.

62. Wang R, Liang D, Liu X, Fan W, Meng S, Cai W. Effect of magnesium ion on polysaccharide fouling. Chem Eng J. 2020;379: 122351.

63. Abrahamse A, Lipreau C, Li S, Heijman S. Removal of divalent cations reduces fouling of ultrafiltration membranes. J Membr Sci. 2008;323(1):153–8.

64. Topuz F, Henke A, Richtering W, Groll J. Magnesium ions and alginate do form hydrogels: a rheological study. Soft Matter. 2012;8(18):4877–81.

Publisher's Note Springer Nature remains neutral with regard to jurisdictional claims in published maps and institutional affiliations.